Inorganic Chemistry

pubs.acs.org/IC

Article

Metal–Metal Bond *Umpolung* in Heterometallic Extended Metal Atom Chains

Amelia M. Wheaton, Jill A. Chipman, Michael D. Roy, and John. F. Berry*

Cite This: *Inorg. Chem.* 2022, 61, 15058–15069

Read Online

ACCESS | Metrics & More | Article Recommendations | Supporting Information

ABSTRACT: Understanding the fundamental properties governing metal–metal interactions is crucial to understanding the electronic structure and thereby applications of multimetallic systems in catalysis, material science, and magnetism. One such property that is relatively underexplored within multimetallic systems is metal–metal bond polarity, parameterized by the electronegativities (χ) of the metal atoms involved in the bond. In heterobimetallic systems, metal–metal bond polarity is a function of the donor–acceptor ($\Delta\chi$) interactions of the two bonded metal atoms, with electropositive early transition metals acting as electron acceptors and electronegative late transition metals acting as electron donors. We show in this work, through the preparation and systematic study of a series of $Mo_2M(dpa)_4(OTf)_2$ (M = Cr, Mn, Fe, Co, and Ni; dpa = 2,2′-dipyridylamide; OTf = trifluoromethanesulfonate) heterometallic extended metal atom chain (HEMAC) complexes that this expected trend in χ can be reversed. Physical characterization via single-crystal X-ray diffraction, magnetometry, and spectroscopic methods as well as electronic structure calculations supports the presence of a σ symmetry $3c/3e^-$ bond that is delocalized across the entire metal-atom chain and forms the basis of the heterometallic Mo_2–M interaction. The delocalized $3c/3e^-$ interaction is discussed within the context of the analogous $3c/3e^-$ π bonding in the vinoxy radical, CH_2CHO. The vinoxy comparison establishes three predictions for the σ symmetry $3c/3e^-$ bond in HEMACS: (1) an *umpolung* effect that causes the Mo–M interactions to become more covalent as $\Delta\chi$ increases, (2) distortion of the σ bonding and non-bonding orbitals to emphasize Mo–M bonding and de-emphasize Mo–Mo bonding, and (3) an increase in Mo spin population with increasing Mo–M covalency. In agreement with these predictions, we find that the Mo_2···M covalency increases with increasing $\Delta\chi$ of the Mo and M atoms ($\Delta\chi_{Mo-M}$ increases as M = Cr < Mn < Fe < Co < Ni), an *umpolung* of the trend predicted in the absence of σ delocalization. We attribute the observed trend in covalency to the decreased energic differential (ΔE) between the heterometal d_{z^2} orbital and the σ bonding molecular orbital of the Mo_2 quadruple bond, which serves as an energetically stable, "ligand"-like electron-pair donor to the heterometal ion acceptor. As M is changed from Cr to Ni, the σ bonding and nonbonding orbitals do indeed distort as anticipated, and the spin population of the outer Mo group is increased by at least a factor of 2. These findings provide a predictive framework for multimetallic compounds and advance the current understanding of the electronic structures of molecular heteromultimetallic systems, which can be extrapolated to applications in the context of mixed-metal surface catalysis and multimetallic proteins.

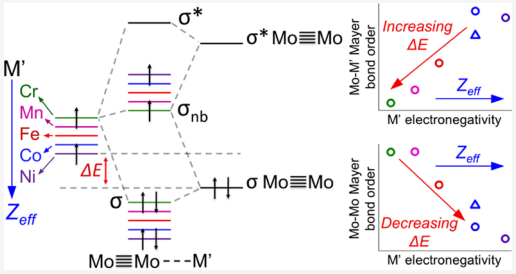

INTRODUCTION

Bond polarity is a fundamental property of chemical systems, with donor–acceptor interactions at the heart of acid–base reactions,[1−4] organic chemistry,[5,6] inorganic solid state chemistry,[7−11] and coordination chemistry.[12−16] For example, the modern lexicon of coordination chemistry now contains X-, L-, or Z-type ligands, which indirectly describes the polarity of a metal–ligand bond by identifying the donor and acceptor involved in the interaction.[17−19] Reversal of expected bond polarity, or *umpolung*, is also an important concept with impacts in organic synthesis,[20−27] catalysis,[6,28−32] frustrated Lewis pairs,[33,34] and bonding in main group chemistry.[35−37] Another area in which bond polarity plays an important but underappreciated role is in coordination compounds containing heterometallic metal–metal bonds. The recent explosion of interest in heterometallic compounds[38−45] has produced a number of systematic series that illustrate how polarity impacts heterometallic bonding generally. Bond polarity is most commonly assessed using electronegativity, χ, and we use here the Allred–Rochow definition,[46] in which χ is effectually proportional to effective nuclear charge, Z_{eff}, according to the following equation

$$\chi = a + \frac{e^2 \cdot Z_{eff}}{r^2}$$

Received: June 17, 2022
Published: September 12, 2022

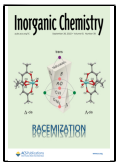

https://doi.org/10.1021/acs.inorgchem.2c02118
Inorg. Chem. 2022, 61, 15058–15069

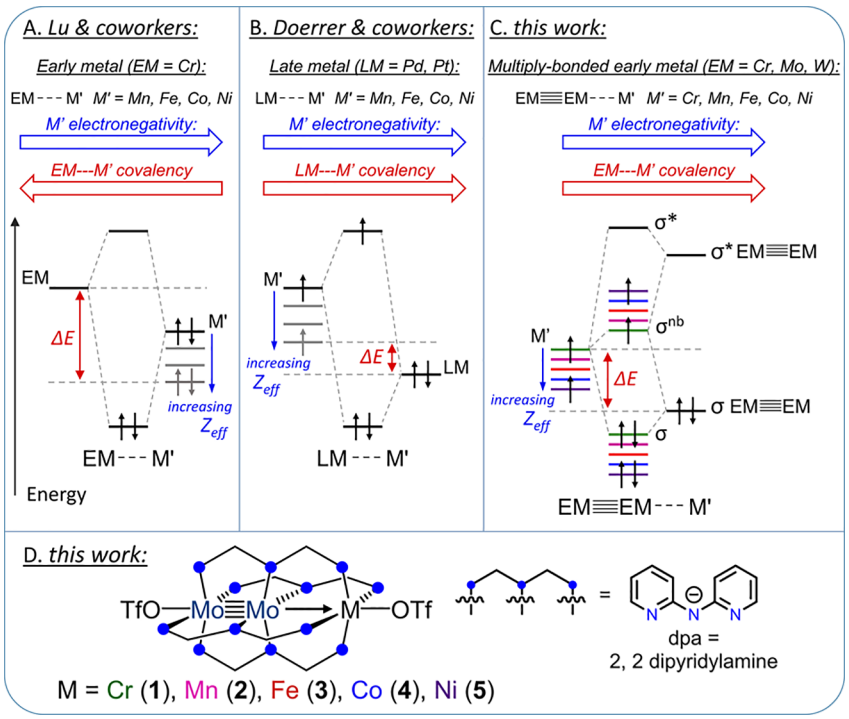

Figure 1. (A) Schematic MO diagram depicting polar metal−metal σ bonding in bimetallics with a static early transition metal and variable later metals. (B) Similar MO diagram for bimetallics with a constant late transition metal and variable early metal. (C) Schematic MO diagram depicting polar metal−metal σ bonding in asymmetric heterotrimetallic extended metal atom chain (HEMAC) complexes with the M≡M group held constant and a variable heterometal. (D) Diagram of the $Mo_2M(dpa)_4(OTf)_2$ HEMAC complexes **1**−**5** studied in this work. The structure of the dpa ligand, 2,2′-dipyridylamide, is shown.

Here, e is the electron charge, r is the atomic radius, and a is a constant that brings the Allred−Rochow scale in line with Pauling's electronegativity scale.

Because χ scales with Z_{eff}, it increases as the transition series is traversed from the early, electropositive metals to the later, more electronegative ones. Thus, in a heterobimetallic complex with a metal−metal bond, the expected bond polarity will have a late metal as a donor and an early metal as an acceptor. For example, Thomas and co-workers have extensively studied the chemistry of Co−Zr bonded compounds, in which they explicitly draw donor−acceptor arrows from the Co to the Zr to emphasize this bond polarity.[47−49] Two further systematic series of compounds serve to illustrate this effect as well.

First, Lu and co-workers have reported many heterobimetallic metal−metal bonded compounds built off of a trisamidoamine-phosphine ligand scaffold.[50−54] Of particular note is their series in which Cr, an early transition metal, occupies the trisamidoamine pocket and a later metal, Mn, Fe, Co, or Ni, occupies the phosphine site (Figure 1A).[54] From a molecular orbital (MO) standpoint of the heterometallic interaction, the Cr atoms act as electron acceptors and the Mn/Fe/Co/Ni atoms serve as donors. With respect to the heterometallic interaction covalency, Ni has the highest χ of the four later metals, resulting in a large energetic mismatch (ΔE) between the frontier d orbitals of the Cr and Ni atoms, and therefore, the Ni atom engages least covalently with the early metal site. Metal−metal bonding thus strengthens with decreasing χ of the heterometal going from Ni to Co to Fe to Mn (Figure 1A) as reflected in the change in the calculated effective metal−metal bond orders (EBO of 0.87 for M′ = Ni; 3.94 for M′ = Mn). While the occupation of metal−metal π- and δ-symmetry antibonding orbitals contributes to the dramatic change in the calculated EBOs, a similar trend of strengthening the metal−metal σ bond with decreasing $\Delta\chi$ (and therefore decreasing ΔE) is also observed for a series of V−M′ (M′ = Fe, Co, Ni) bimetallics[51] as well as for other bimetallic complexes containing early transition metals of Ti[55,56] and Nb.[57] These series help substantiate the assessment that the $\Delta\chi$ between the two metal atoms needs to be considered when assessing the corresponding metal−metal bond covalency.

Another illuminating set of compounds has been reported by Doerrer and co-workers, who have used thiocarboxylate ligands to support heterometallic interactions featuring the late transition metal Pt and a variable first-row heterometal M, where M = Mn, Fe, Co, and Ni (Figure 1B).[58,59] Here, Pt is the donor and the Mn/Fe/Co/Ni atoms are the acceptors. In this set of compounds, the Pt−Mn pair is the least covalent and Pt−M bonding becomes stronger with decreasing $\Delta\chi$ going from Mn to Fe to Co and Ni and decreasing ΔE. As in the case of the Cr/V heterobimetallics, $\Delta\chi$ and ΔE are directly correlated, and decreasing the energetic mismatch in orbital energies leads to greater heterometallic covalency.

In contrast to the aforementioned bimetallic systems, our research group has utilized HEMAC complexes to probe heterometallic metal−metal interactions within multimetallic systems.[40] Broadly defined, HEMAC complexes contain a linear chain of three metal atoms in idealized C_4 symmetry and are supported by a helical arrangement of bridging equatorial 2,2′-dipyridylamido ligands (dpa, Figure 1D). Specifically, the HEMAC complexes that our work focuses on have a general formula of $M_2M'(dpa)_4X_2$, where M_2 represents two quadruply bonded early transition metal atoms (M = Cr, Mo, or W) and M′ is a third, paramagnetic, divalent transition metal ion

https://doi.org/10.1021/acs.inorgchem.2c02118
Inorg. Chem. 2022, 61, 15058−15069

typically from the first row of the transition series. X is a halide or pseudohalide axial ligand.

The key bonding feature of HEMACs is the three-center/three-electron ($3c/3e^-$) bond formed via overlap of the three d_{z^2} orbitals of the three metal atoms in the chain. If all three metal atoms have the same identity, then the bonding scheme becomes analogous to $3c/3e^-$ bonded systems such as H_3 or the π system of the allyl radical, as was pointed out by Bénard and co-workers in 2001.[60] For HEMACs, the most straightforward comparison is to the vinoxy radical, CH_2CHO, though to our knowledge this bonding analogy has not been explored before. A comparison of the relevant orbital pictures is given in Scheme 1. The three atomic orbitals

Scheme 1. Schematic Diagram Comparing the Bonding (b.), Non-Bonding (n.b.), and Antibonding (a.b.) MOs of the Three-Center Interaction in HEMAC Complexes (Left) and the Vinoxyl Radical (Right)[a]

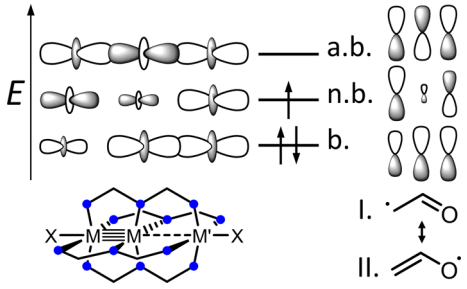

[a]M = early transition metal (Cr, Mo, or W), M′ = heterometal ion, X = anionic axial ligand.

(d_{z^2} for HEMAC and p for vinoxy) combine to form three MOs of bonding, non-bonding, and antibonding character that are filled with the three available valence electrons of the system. For the vinoxy system, one expects a C−C bond to be more covalent than a C−O bond because O has higher Z_{eff} than C. However, the three-center nature of the bonding results in polarity *umpolung* where the C−O π bond is more covalent than the C−C π bond and therefore resonance structure **I** is favored over **II** in the ground state.[61] From an MO standpoint, this polarity *umpolung* is manifested as the π bonding orbital combination having a larger contribution from the O atom than the terminal C atom. The non-bonding combination has a small amount of central C character (rather than a node as in the allyl radical), which is slightly π bonding with respect to the C−C bond and π antibonding with respect to the C−O bond. The main radical character of vinoxy, therefore, is localized on the terminal C atom rather than the O atom.

Analogy of the π bonding in vinoxy to the $3c/3e^-$ bond in HEMAC complexes is straightforward if we substitute the C atoms of vinoxy for the metal atoms of the quadruple bond and the O atom for the heterometal ion. Using the first reported HEMAC, $Cr_2Fe(dpa)_4Cl_2$, as a representative example,[62] the two *individual* Cr^{2+} ions are more electropositive than the Fe^{2+} ion. Based on the expected correlation of $\Delta\chi$ and ΔE described above for bimetallic systems, one would expect Cr ← Fe bond polarity. However, like the C p orbitals of vinoxy, the valence d orbitals of the two Cr^{2+} ions combine to form a set of bonding (σ, 2 × π, δ) and antibonding (σ^*, 2 × π^*, δ^*) MOs that are energetically stabilized and destabilized, respectively, relative to those of the Fe^{2+} ion. The filled σ-symmetry Cr_2 MO, formed via a collinear combination of two Cr d_{z^2} atomic orbitals, could therefore serve as an electron pair donor (i.e., a dative "ligand") to the more electronegative Fe, resulting in an *umpolung* of the Cr−Fe interaction and a Cr → Fe bond polarity.

Comparison to vinoxy allows us to make three important predictions about HEMACs: (1) the *umpolung* effect should cause the M−M′ interactions to become more covalent as the Z_{eff} of M′ increases (Figure 1C), (2) increasing M−M′ covalency should lead to distortion of the nonbonding orbital such that it takes on M−M bonding and M−M′ antibonding character, and (3) increasing M−M′ covalency should increase the spin population of the terminal M atom. However, despite extensive development of HEMAC chemistry,[40,63−67] the use of this framework for understanding the polarity of heterometallic interactions within HEMAC complexes (and more broadly within multimetallic systems) has not been explored fully. These efforts have in the past been hampered by the lack of a synthetic method to access a complete and systematic series of $M_2M'(dpa)_4X_2$-type complexes with a varied scope of heterometal ions, as well as the multireference nature of the Cr−Cr multiple bond,[68,69] which prevented us from fully interrogating the HEMAC complexes computationally. Thus, complete validation of this framework for understanding the trend in covalency of the metal−metal interactions in HEMAC complexes requires investigation of a broad, systematic series of $M_2M'(dpa)_4X_2$-type complexes that are both synthetically accessible and computationally tractable, which is now accomplished in the work reported here.

In this work, we report the preparation of a novel series of $Mo_2M(dpa)_4(OTf)_2$ HEMACs. We chose the $Mo_2M(dpa)_4(OTf)_2$ HEMACs as targets due to the synthetic utility reported for $Mo_2Ni(dpa)_4(OTf)_2$ (**5**).[70] The $Mo_2M(dpa)_4(OTf)_2$ HEMACs are challenging synthetic targets due to the presence of the labile OTf^- ligands, which contributes to extreme air sensitivity of several members of the series. Nevertheless, we report the successful synthesis and characterization of $Mo_2M(dpa)_4(OTf)_2$ HEMACs with heterometals M = Cr, Mn, Fe, and Co (**1**, **2**, **3**, and **4**, Figure 1C,D) to complement the more stable **5** that we previously reported.[70] Electronic structure calculations reveal that the Mo_2 σ MO does indeed act as a ligand-like electron pair donor to the third heterometal ion, with Mo_2−M′ covalency increasing with the Z_{eff} of the heterometal ion. This increase in covalency stems from a decrease in the ΔE between the Mo_2 σ bonding MO and the d_{z^2} orbital of the heterometal ion. The decreasing ΔE, in turn, is the result of an increase in $\Delta\chi_{Mo-M'}$, in direct opposition to the influence of $\Delta\chi$ in previously reported heterobimetallic systems with early transition metals. Comparison to the $Mo_2M(dpa)_4Cl_2$ series reveals that this heterometallic *umpolung* is a broader trend among HEMAC complexes and whose characteristics are analogous to the π bonding in the vinoxy radical. These results provide straightforward guiding principles that may be used to understand and modulate the covalency of metal−metal bonds within other types of multimetallic systems, such as those involved in surface catalysis[43,71,72] or metalloenzyme active sites.[73−81] They are also relevant within the context of studies devoted to ennobling Earth-abundant base metals for various applications,[82−88] as in this work we demonstrate that the early transition metal Mo can take on electronegativity characteristics of a later transition metal (e.g., Pt) when participating in a metal−metal multiple bond.

https://doi.org/10.1021/acs.inorgchem.2c02118
Inorg. Chem. 2022, 61, 15058−15069

RESULTS AND DISCUSSION

Synthesis. *M(OTf)$_2$ Salts.* Compound **5** is best prepared via reaction of $Mo_2(dpa)_4$ with 1.5 equiv of $Ni(OTf)_2$.[70] Use of an analogous synthetic route for other $Mo_2M(dpa)_4(OTf)_2$ HEMACs is complicated by the fact that $Cr(OTf)_2$ is not commercially available and that other anhydrous $M(OTf)_2$ salts, despite being commercially available, are inconsistently characterized[89] and in our hands give inconsistent results. We therefore considered several methods for preparing $M(OTf)_2$ starting materials,[89−93] ultimately settling on the precipitation of an insoluble salt.[89,91] We found that reaction of MCl_2 (M = Cr, Mn, Fe, Co, and Ni) with 2.0 equiv of TlOTf in CH_3CN affords the $M(OTf)_2$ salts in good yields and high purity (Scheme 2A). This preparation involves the initial formation of

Scheme 2. Overview of the Synthetic Methods Used for This Work (A) Preparation of the M(OTf)$_2$ Salts. (B) Preparation of 1, 3, 4, and 5. (C) Preparation of 2

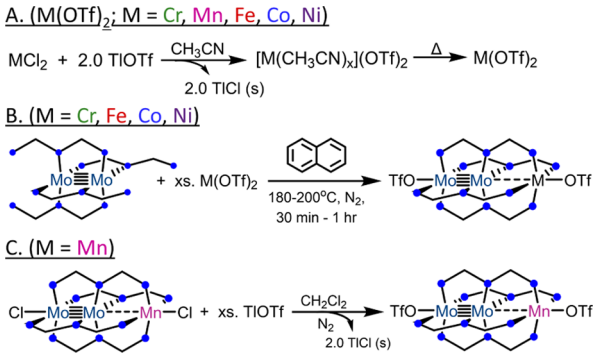

a soluble, heteroleptic $M(CH_3CN)_x(OTf)_2$ complex and precipitation of TlCl. After filtration and drying, stretches in the 2300 cm^{-1} range of the infrared (IR) spectra indicate residual CH_3CN coordination to the $M(OTf)_2$ salt (Figure S1).[93] Further drying of these powders under vacuum for 12 h at 80 °C afforded the rigorously solvent-free $M(OTf)_2$ salts as demonstrated by disappearance of the nitrile stretches in the IR (Figure S2) as well as by elemental analysis. The $M(OTf)_2$ salts were also characterized for the first time by ^{19}F NMR spectroscopy in CD_3CN solutions (Figure S3), and the spectra indicate an equilibrium between metal-bound and free triflate. The $Fe(OTf)_2$ precursor was also characterized by Mossbauer spectroscopy (Figures S4 and S5) and is consistent with the previously reported spectrum of the compound prepared by reaction of triflic acid and Fe metal.[94,95] Ultimately, we observe that using the $M(OTf)_2$ salts prepared by our synthetic method for preparation of the heterometallic complexes as described below improves overall product purity and reaction yields.

Heterometallic Complexes. **1**, **3**, and **4** were straightforward to prepare in an analogous manner to the synthetic route we previously used to access **5** (Scheme 2B). However, all attempts to prepare **2** using a molten naphthalene route failed to provide an analytically pure crystalline product. Instead, this general method afforded a green-brown powder that was characterized by UV−vis (Figure S6) and IR spectroscopies (Figure S7). The electronic absorption spectra of the powder material in CH_2Cl_2 shows a broad feature at 800 nm corresponding to the reported energy and characteristic shape of the $\delta \rightarrow \delta^*$ transition of the $[Mo_2(dpa)_4]^+$ cation.[96] The IR spectrum contains stretches corresponding to the $Mo_2(dpa)_4$[67] unit as well as stretches at 1030 and 623 cm^{-1} that are characteristic of a triflate SO_3 moiety.[90] This green-brown powder is therefore likely a mixture of **2** and $[Mo_2(dpa)_4][OTf]$. We were unable to isolate or characterize any monometallic Mn^{II} containing products; however, we hypothesize that the $Mn^{II}(OTf)_2$ reagent can act as an oxidant to the $Mo_2(dpa)_4$, forming $[Mo_2(dpa)_4][OTf]$- and $Mn^{I}(\eta_6\text{-}C_{10}H_8)_2$-type complexes, which are well known.[97−99]

An alternative synthetic route for **2** was therefore developed and employed based upon the observation that **5** could be prepared via reaction of $Mo_2Ni(dpa)_4Cl_2$ and 2 equiv of TlOTf.[70] A slow but steady color change from brown to green is observed upon stirring $Mo_2Mn(dpa)_4Cl_2$ in CH_2Cl_2 with excess TlOTf for 2 weeks (Scheme 2C). The sparing solubility of TlOTf in CH_2Cl_2 limits the reaction rate and yields of **2**.

Crystallography. In this work, the entire $Mo_2M(dpa)_4(OTf)_2$ (M = Cr, Mn, Fe, Co, Ni) series has now been structurally characterized via X-ray crystallography (Tables S1 and S2). A representative structure is shown in Figure 2, with the other structures shown in the Supporting Information. The complete structural characterization of the $Mo_2M(dpa)_4(OTf)_2$ series also invites comparison to the structures of the $Mo_2M(dpa)_4Cl_2$ [M = Cr (**6**),[63] Mn (**7**),[100] Fe (**8**),[66] Co (**9**),[67] and Ni (**10**)[101]] series, reported elsewhere and whose distances are reproduced in Table S3. Table S2 also contains the density-functional theory (DFT) optimized geometric parameters for the $Mo_2M(dpa)_4(OTf)_2$ HEMACs with the M^{2+} ions, and in general, the calculated geometries are in good agreement with the experimental ones. This provides support for the computational methods employed in the spectroscopic and electronic structure analyses of the $Mo_2M(dpa)_4(OTf)_2$ HEMAC complexes, described later.

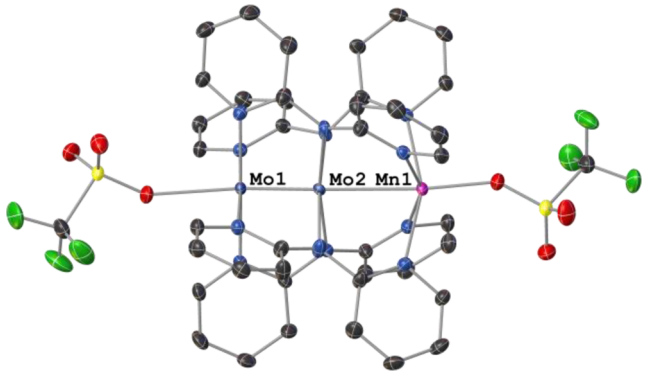

Figure 2. Molecular drawing of **2** with selected atom labels. All atoms are shown at 50% probability levels; all H atoms and minor disordered components are omitted for clarity.

Focusing on the heterometallic interactions in **1**−**10**, we see a steady decrease in Mo−M distance across both series from M = Mn to Ni. The low-spin compound **4**, as well as the Cr compounds, have anomalously short Mo−M distances. One possible reason for the general contraction in Mo−M distance is the decreasing size of the M atoms. However, the contraction in Mo−M distance, Δd_{Mo-M} = 0.26 to 0.27 Å, is steeper than the contraction in M−N distances, Δd_{M-N} = 0.08 to 0.10 Å. The M−X distances to the axial OTf in **2**−**5** or Cl in **7**−**10** actually increase slightly by 0.07 Å, a possible *trans* influence of the shorter Mo−M interaction. It is therefore reasonable to assign a degree of covalency to the Mo−M bonds, which increases as M is changed from Mn to Ni.

https://doi.org/10.1021/acs.inorgchem.2c02118
Inorg. Chem. 2022, 61, 15058−15069

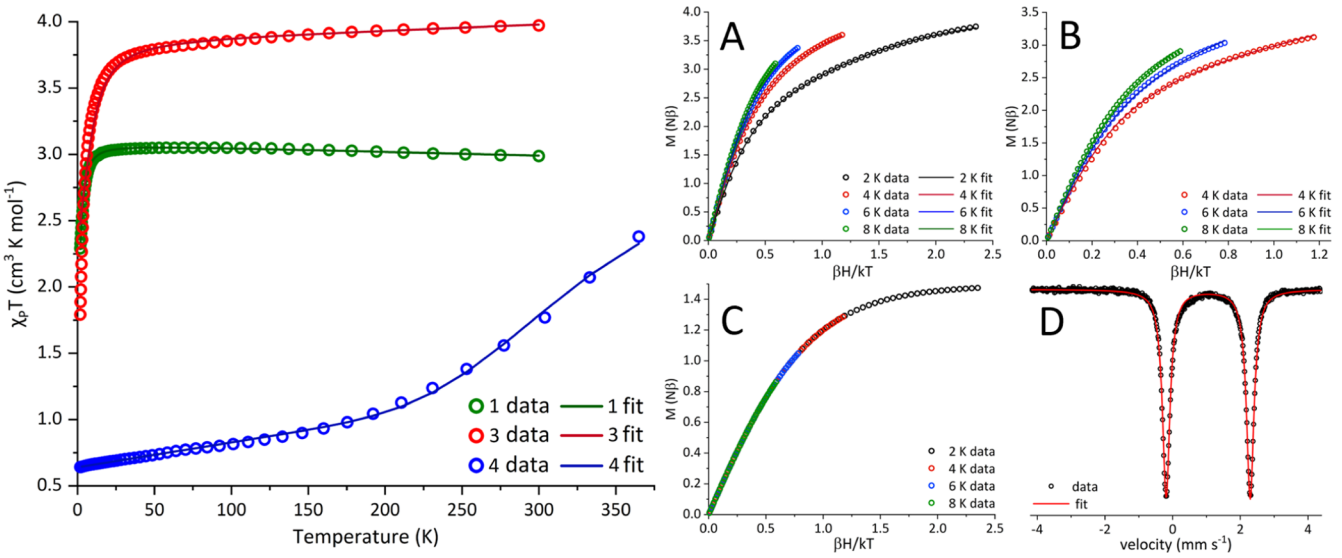

Figure 3. Left: Magnetic susceptibility data and fits for **1**, **3**, and **4**. Right (counterclockwise from top left): reduced magnetization data and fits for **1** (A), **3** (B), and **4** (C, data not fitted). The Mössbauer spectrum of **3** at 80 K is shown in the figure on the bottom right (D): δ = 1.05 mm/s, ΔE_Q = 2.48 mm/s, Γ = 0.27 mm/s, χ^2 = 2.37; δ(calc.) = 0.93 mm s^{-1}; ΔE_Q(calc.) = 3.33 mm s^{-1}.

SQUID Magnetometry and EPR Spectroscopy. Comparison to the vinoxy radical suggested that the outer Mo atom of the metal−metal quadruple bond in **1**−**5** would display some paramagnetic character. However, as has been observed for the $[Mo_2Ni(dpa)_4Cl_2]^+$ cation,[101] the σ-symmetry spin delocalization will reinforce the spin on M additively and would therefore not be detectable by SQUID magnetometry. Thus, for the purpose of modeling the magnetic susceptibility data, the paramagnetism of the heterometal ion is the dominant feature and **1**−**5** may be considered to a first-order approximation to contain a diamagnetic Mo_2 quadruply bonded unit attached to a paramagnetic metal site. For example, **5** was previously described as having an S = 1 ground spin state stemming from the high-spin Ni^{2+} ion.[70] To establish the spin states of the paramagnetic metals in **1**, **3**, and **4** (low yields of **2** prevented physical measurements), magnetic susceptibility, EPR, and Mössbauer spectroscopies are used. Magnetic susceptibility and reduced magnetization measurements for **1**, **3**, and **4** are shown in Figure 3 (Table 1 for fitting parameters), and EPR spectra of **4** at 10 K are shown in Figure 4. The Mössbauer spectrum of **3** is also shown in Figure 3.

The measured values of χ_PT at 300 K (Figure 3) for **1** and **3** are 2.98 and 3.97 cm^3 K mol^{-1}. These values are consistent with S = 2 systems with g-factors slightly below and moderately above g = 2 and are expected for systems with less than and greater than five valence d electrons, respectively. The sharp downturn of the $\chi_P T$ values at low temperatures and nested variable temperature magnetization curves for **1** and **3** (Figure 3A,B) are consistent with strong magnetic anisotropy that can be modeled as zero-field splitting (ZFS). The data for both **1** and **3** were fitted with axial ZFS parameters with D < 0 for both HEMACs. The value of D for **1** (−2.052 cm^{-1}) is slightly smaller than that of **6** (−2.187 cm^{-1}).[89] For **3**, D is slightly smaller in magnitude and opposite in sign to that of $Cr_2Fe(dpa)_4Cl_2$ (D = 8.3 cm^{-1}).[62] The sign and magnitude of D for **1** and **3** match those predicted from the DFT-modeled electronic structure (Table 1, vide infra). The negative values for D_{calc} and the small values of E_{calc} (ca. 0.01 cm^{-1}) indicate easy-axis anisotropy of the Cr and Fe sites in **1** and **3**, with an elongation along the metal−metal axis.[102−104] The electron delocalization through the Mo−Mo−M chain likely contrib-

Table 1. SQUID Fit Parameters for 1, 3, and 4

	1	3		4
$g_\parallel$	1.9332(6)	2.32(1)	g_{LS}	2.23[b]
$g_\perp$	2.0704(3)	2.152(3)	g_{HS}	2.53[c]
D (cm^{-1})	−2.052(3)	−6.42(8)	ΔH	15.7(5)
D_{calc} (cm^{-1})	−3.132	−3.375	T_C	339(2) K
E_{calc} (cm^{-1})	0.008	0.016	P_{HS}	6.8(1)%
TIP	−0.00029(6)	0.0004(1)	TIP	0.00201(4)
residual[a]	0.000034	0.1016		

[a]Residual = $\left[\sum_{i=1}^{points}(M_{exp}-M_{calc})^2\right]\left[\sum_{i=1}^{points}(\chi_{exp}-\chi_{calc})^2\right]$; where M_{exp}/M_{calc} = measured/calculated magnetization and χ_{exp}/χ_{calc} = measured/calculated susceptibility. [b]Fixed to the value determined by EPR. [c]Fixed to the g value determined for **9**.

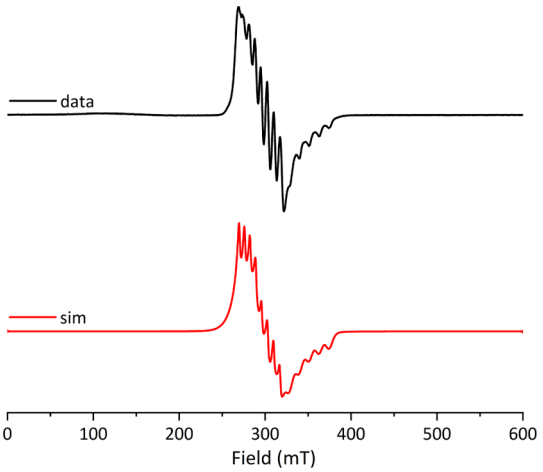

Figure 4. X-band EPR spectrum of **4**; frequency = 9.38 MHz, temperature = 10 K. Simulation parameters: [g_x, g_y, g_z] = [2.34, 2.25, 2.01]; [A_x, A_y, A_z] = [160, 230, 322] MHz; H-strain = [700, 100, 200] MHz.

https://doi.org/10.1021/acs.inorgchem.2c02118
Inorg. Chem. 2022, 61, 15058−15069

Table 2. Comparison of the Electronic Properties of the Co^{2+} Ions in $M_2Co(dpa)_4X_2$ HEMACs[a]

compound	S (Co^{2+})	ΔH (kJ mol^{-1})	ΔS (J mol^{-1} K^{-1})	refs
4 (M = Mo, X = OTf^-)	1/2 → 3/2	15.7(5)	46	this work
$Mo_2Co(dpa)_4Br_2$	1/2 → 3/2	13.95	67	106
9 (M = Mo, X = Cl^-)	3/2	n/a	n/a	67
$Cr_2Co(dpa)_4Cl_2$	1/2 → 3/2	5.7	27	67

[a] S = spin state of the Co^{2+} ion, where 1/2 → 3/2 indicates spin-crossover behavior, ΔH = enthalpy difference between low and high spin states, and ΔS = entropy difference between low and high spin states.

utes to this axial anisotropy. This idea is further supported by the observed magnetic anisotropy of $M_2Cr(dpa)_4Cl_2$ systems where the magnitude of D increases in the order Cr < Mo < W. This increase is consistent with an increase in spin−orbit coupling (i.e., the heavy ion effect), in which the M≡M unit is considered as a ligand to the paramagnetic site.[105]

The Mössbauer spectrum of **3** displays an isomer shift, δ = 1.05 mm s^{-1}, and quadrupole splitting, ΔE_Q = 2.48 mm s^{-1}, similar to that reported for the Mössbauer spectrum of **8** (δ = 1.02 mm s^{-1} and ΔE_Q = 2.02 mm s^{-1})[66] and supports the assignment of a high spin S = 2 ion in the trimetallic complex. The good agreement between measured and DFT-calculated Mössbauer parameters for **3** [δ(calcd) = 0.93 mm s^{-1}; ΔE_Q(calcd) = 3.33 mm s^{-1}] provides further support for the calculated electronic structure discussed in more detail below. Notably, the ΔE_Q for **3** is substantially larger than that of the $Fe(OTf)_2$ precursor (ΔE_Q = 2.04 mm s^{-1}, Figure S4), indicating an increase in the electric field gradient about the Fe nucleus in **3** in the presence of the Mo_2 metalloligand. This increased asymmetry is consistent with the axial anisotropy observed for **3** in the SQUID magnetometry measurements.

Crystallographic data at 100 K, particularly the short Co−N bond lengths, suggest that the Co^{2+} ion in **4** is low spin, S = 1/2, which is consistent with the measured χ_PT (ca. 0.6 cm^3 K mol^{-1}) at the low temperature limit (spin-only: $\chi \cdot T$ = 0.375 cm^3 K mol^{-1}). This assignment is also corroborated by superimposable reduced magnetization curves (Figure 3C) and the lack of a downturn in χ_PT at low temperatures, which, taken together, indicate that there is no ZFS present for **4**, as an S = 1/2 state is not subject to ZFS. The X-band EPR spectrum of **4** at 10 K shows one major slightly rhombic signal centered at g_{avg} = 2.23. The observed g-value and extensive hyperfine (due to coupling with the I = 7/2 ^{59}Co nucleus) is consistent with an S = 1/2 ground state. Above 150 K, however, the χ_PT data for **4** increases steeply toward a value of 2.5 cm^3 K mol^{-1} at 300 K. This behavior cannot be explained by the S = 1/2 ground state or by temperature-independent paramagnetism (an effect that would be present at all temperatures). The most plausible explanation for the high-temperature magnetic data is that **4** displays partial spin crossover, where thermal energy can populate the higher S = 3/2 spin state. The parameters that resulted from fitting the magnetic susceptibility data for **4** are listed in Table 1, and further discussion of the spin-equilibrium model used for the fit can be found in the Supporting Information.

Three previous HEMAC complexes with Co^{2+} heterometals have been characterized via SQUID magnetometry, and **4** is the third to display spin-crossover behavior. A summary of these results is outlined in Table 2. For all three HEMAC complexes with spin-crossover behavior, ΔS is positive, as a result of the high-spin state having more degrees of freedom than its low-spin counterpart. Compound **9** is the only HEMAC with a high spin, S = 3/2 Co^{2+} ion at all temperatures; as such, ΔH < 0 and cannot be measured. For **4**, the ΔH needed to overcome spin pairing is 15.7 kJ/mol, which is higher than those of all of the other HEMACs, which bear π-donating (and thus weaker field) axial halides.

Electronic Absorption Spectroscopy. Electronic absorption spectra for **1**, **3**, **4**, and **5** in CH_2Cl_2 show three major transitions at ca. 420 nm (A), 550 nm (B), and 630 nm (C) (Figure 5, Table S4). Time-dependent DFT (TDDFT) studies

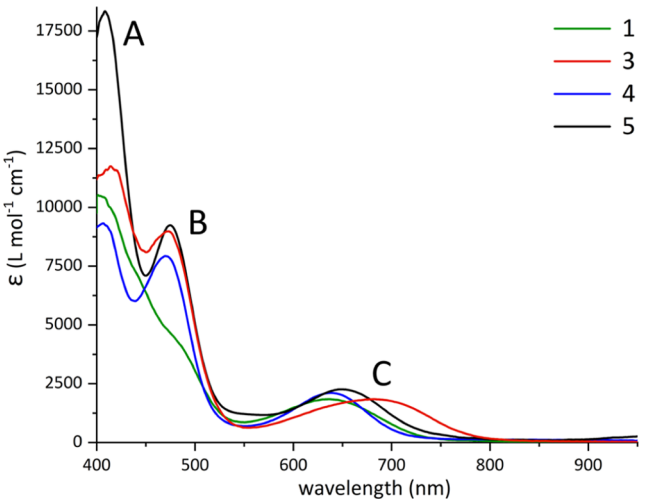

Figure 5. Electronic absorption spectra for **1**, **3**, **4**, and **5**.

of **5** indicated that the major contributions to the A and B transitions arise from Mo≡Mo δ donation to the pyridyl rings of the dipyridylamine ligand (metal to ligand charge transfer, or MLCT) while a Mo≡Mo $\delta \rightarrow \delta^*$ transition gives rise to the lower energy and weaker intensity C bands.[70] The similarity of transition intensities and band shapes indicate a similar assignment of the A, B, and C transitions for all four compounds as MLCT (A and B) and $\delta \rightarrow \delta^*$ (C). Assignment of the low-energy features as Mo≡Mo $\delta \rightarrow \delta^*$ transitions (with the exception of **3**; see below) is supported by TDDFT calculations as shown in Figure S18. The differences between calculated and experimental transition energies are of a similar magnitude to that observed for other HEMAC complexes.[63,70]

Transition C for **3** deserves special comment, as it is red-shifted and broadened compared to the other HEMACs.[66] Calculations on **3** indicate that the experimental C transition corresponds to a feature at 910 nm in the calculated spectrum (Figure S18 inset) that corresponds to a Fe d_{xy} → Mo≡Mo δ^* transition (Figure S19). This assignment is consistent with the calculation of a doubly occupied δ symmetry Fe d_{xy}-based MO that is higher in energy than the Mo≡Mo δ orbital (Figure S24). Additionally, the calculated 910 nm feature also has two Fe d_{xy} → dpa π^* transitions as the other major contributors to its calculated intensity instead of Mo≡Mo $\delta \rightarrow \delta^*$-based

https://doi.org/10.1021/acs.inorgchem.2c02118
Inorg. Chem. 2022, 61, 15058−15069

transitions. This effect is unique to the Fe compound, as the Co d_{xy} orbital in **4** is lowered below the energy of the Mo_2 δ orbital due to increased Z_{eff} (Figure S25).

Electronic Structure. Single-point DFT calculations of **1**−**5** were performed in order to determine the nature of the metal−metal bonding in **1**−**5** and to allow comparison to **6**−**10**. The $Mo_2M(dpa)_4X_2$ (X = anionic axial ligand) HEMACs have similar electronic structures, the basis of which can be understood by a ligand field theory (LFT) description of the Mo≡Mo quadruple bond, particularly its low-energy, filled σ-symmetry component, acting as an electron-pair donor to the heterometal ion within a C_4 symmetric ligand field.

Figure 6 presents a representative MO diagram using this treatment on the Mo≡Mo···Cr complex. The four lowest

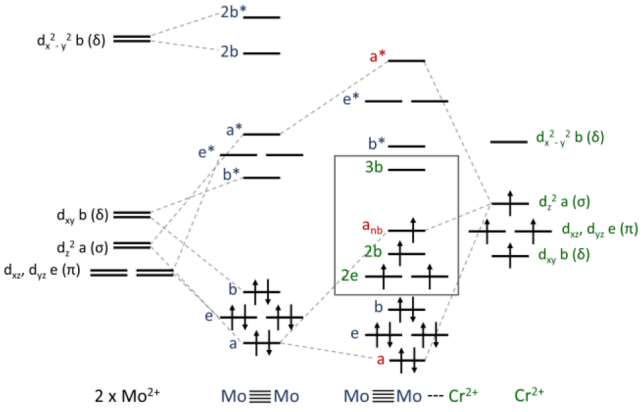

Figure 6. Ligand field theory treatment of metal−metal bonding in asymmetric HEMAC complexes. The dark gray box is used to emphasize the HEMAC MOs that involve the heterometal d orbitals.

occupied and four highest unoccupied energy MOs of the HEMAC are Mo≡Mo based and conform to the σ, two π, and δ bonding and antibonding orbitals of the Mo≡Mo quadruple bond with *a*, *e*, and *b* symmetry, respectively, in the C_4 point group. The middle five MOs receive their predominant contribution from the five d orbitals of the Cr^{2+} ion (two δ orbitals, each of *b* symmetry, two *e*-symmetry π orbitals, and the σ orbital of *a* symmetry). The Mo≡Mo π and the δ orbitals of *e* and *b* symmetry are of the proper symmetry to overlap with *e*- and *b*-symmetry orbitals on Cr, but the spatial overlap is not effective. Thus, these sets of orbitals are primarily localized to the Mo≡Mo or to Cr, respectively. The *a*-symmetry d_{z^2} orbitals, conversely, overlap sufficiently well to form bonding, non-bonding, and antibonding σ-symmetry combinations. The doubly occupied σ and singly occupied σ_{nb} orbitals form a $3c/3e^-$ bond that is delocalized across the entire metal-atom chain. As outlined in the Introduction, with comparison to the vinoxy radical, in EMACs and symmetric HEMACs, the σ_{nb} orbital node is on the central metal atom (Scheme 1). For asymmetric HEMACs, the exact placement of this node varies with the identity of the heterometal.

This MO picture is complicated by the fact that **1**−**5** possess C_1, not C_4, symmetry. However, our calculated results (see Figures S22−S27 for MO diagrams for **1**−**5**) do conform to our expectations from this LFT model and thus validate the use of this framework for the discussion herein. For **1**−**5**, the δ and π symmetry orbitals are localized to either the Mo_2 quadruple bond or the paramagnetic heterometal. Notably, the singly occupied orbitals (with exception of the σ_{nb}, vide infra) are heterometal based. This is consistent with our observation that the magnetic behavior of **1**−**5** is well modeled under the assumption of a diamagnetic Mo_2 moiety and an isolated, paramagnetic heterometal ion.

The isosurface plots and metal atom contributions to the β σ and σ_{nb} orbitals are shown in Figure 7 (see Figure S20 for α component contributions, which, due to spin polarization, suffer from substantial ligand contributions that obfuscate the analysis of metal contributions). For **1**−**5**, the lowest-energy σ MO is primarily Mo≡Mo in character, while the σ_{nb} orbital is primarily of heterometal character. This situation arises from the relative stability and strength of the σ bonding contribution of the Mo≡Mo quadruple bond, leaving it significantly lower in energy than the heterometal ion's σ-symmetry d_{z^2} orbital. As the energetic difference (ΔE) between the Mo_2 σ orbital and the heterometal d_{z^2} orbital decreases, the Mo_2 contribution to the three-center σ_{nb} orbital increases. These contributions are predicted by the LFT model and the analogy to the vinoxy radical, as the filled Mo≡Mo σ-component acts as a "metalloligand" to the heterometal ion; the reproduction of this effect by DFT lends credence to these models.

The extent of delocalization, or covalency, of the $3c/3e^-$ σ bond therefore depends on the identity of the heterometal ion in the metal-atom chain. We calculate a gradual increase in the heterometal ion's contribution to the β σ orbital (from ca. 13.2 to 37.7%) moving from the left to the right across the periodic table. The calculated trends indicate a polarization of the $3c/3e^-$ metal−metal bond toward the heterometal ion with increasing Z_{eff} of the heterometal ion (Cr < Mn < Fe < Co < Ni). This polarization also corresponds to an increase in the Mo_2···M antibonding character in the σ_{nb} orbital, with the contribution of the central Mo atom to the β σ_{nb} orbital increasing from ca. 2.0 to 12%. This shift from a truly non-bonding to a relatively Mo_2···M antibonding σ_{nb} MO can be rationalized as an increase in the energetic destabilization of the σ_{nb} MO with an increase in the covalency of the Mo_2···M interaction. In the most covalent case, the Mo_2−Ni σ and σ_{nb} orbitals are highly reminiscent of the $3c/3e^-$ π and π_{nb} orbitals of vinoxy radical (Scheme 1). The trends in polarization of both the σ and σ_{nb} MOs can be understood as an increase in the heterometallic bond covalency with increased Z_{eff} of the heterometal. Specifically, increasing the Z_{eff} of the heterometal ion (i.e., increasing the Mo−M $\Delta\chi$) stabilizes the heterometal d orbitals, bringing them closer in energy to the bonding MOs of the Mo≡Mo metalloligand, decreasing the energetic difference ΔE between the two contributors as we originally outlined in Figure 1C. The improved energetic overlap strengthens the Mo_2···M interaction, resulting in a polarization of the σ and σ_{nb} MOs (with Mo_2···M antibonding interactions) toward the increasingly electronegative heterometal and a more covalent $3c/3e^-$ bond. Comparison of **1**−**5** with **6**−**10** supports this analysis, as the σ and σ_{nb} orbital contributions follow the same general trends (Figure S21), with the **6**−**10** orbitals also having significant contributions from the Cl p_z orbitals. The most pronounced discrepancies in the calculated contributions are between **4** and **9**, which are expected given that the two Co^{2+} ions have different ground spin states. The observation of polarization of the σ MOs for both series indicates that the heterometal ion can be used to modulate the covalency of the $3c/3e^-$ metal−metal bond independent of the choice of axial ligand.

The calculated Mayer bond orders (MBO) for the Mo≡Mo and Mo−M bonds provide an unambiguous display of the

https://doi.org/10.1021/acs.inorgchem.2c02118
Inorg. Chem. 2022, 61, 15058−15069

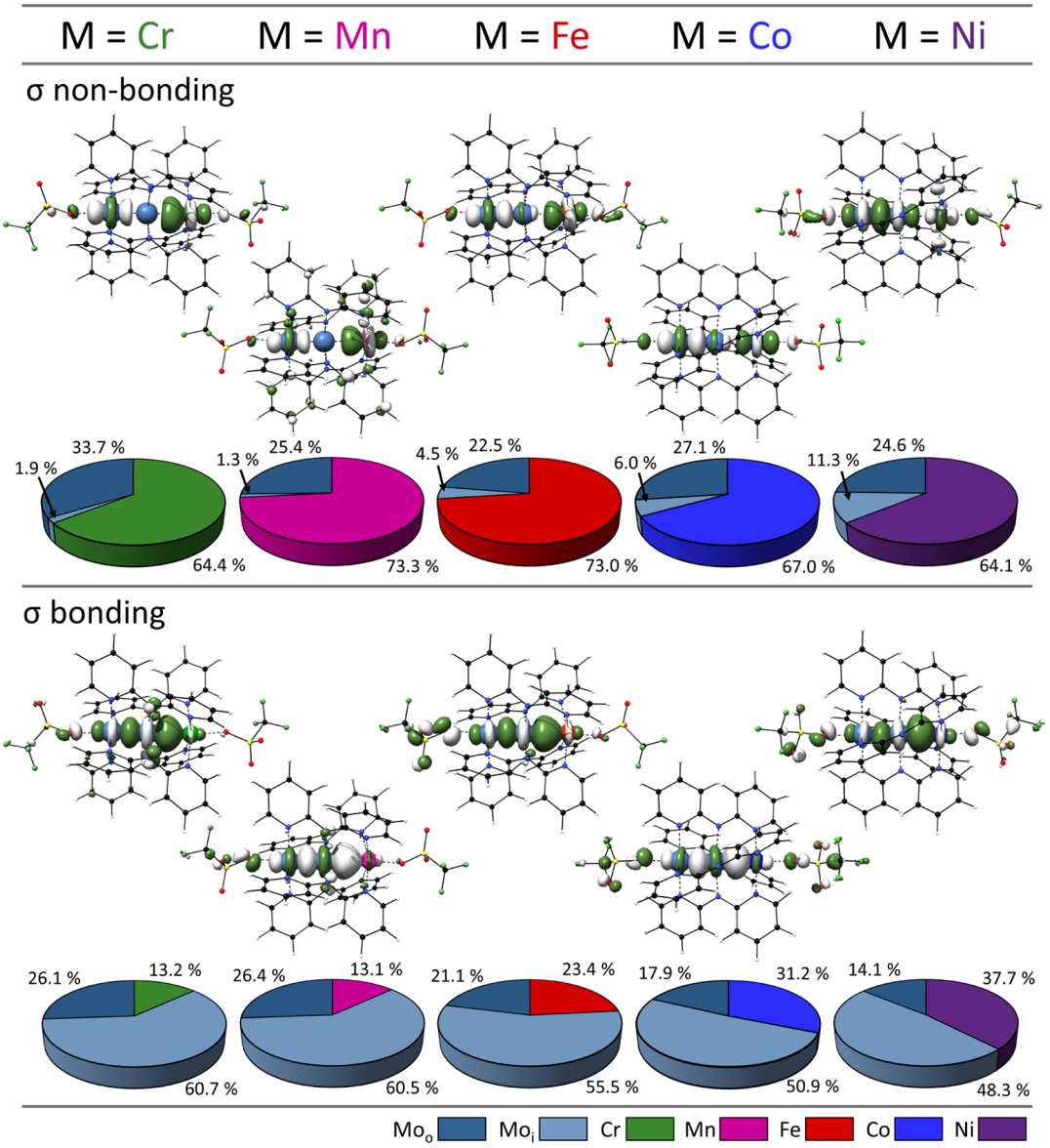

Figure 7. Isosurface plots and orbital occupations for the β components of the σ and σ_{nb} orbitals of (from left to right) **1**, **2**, **3**, **4**, and **5**.

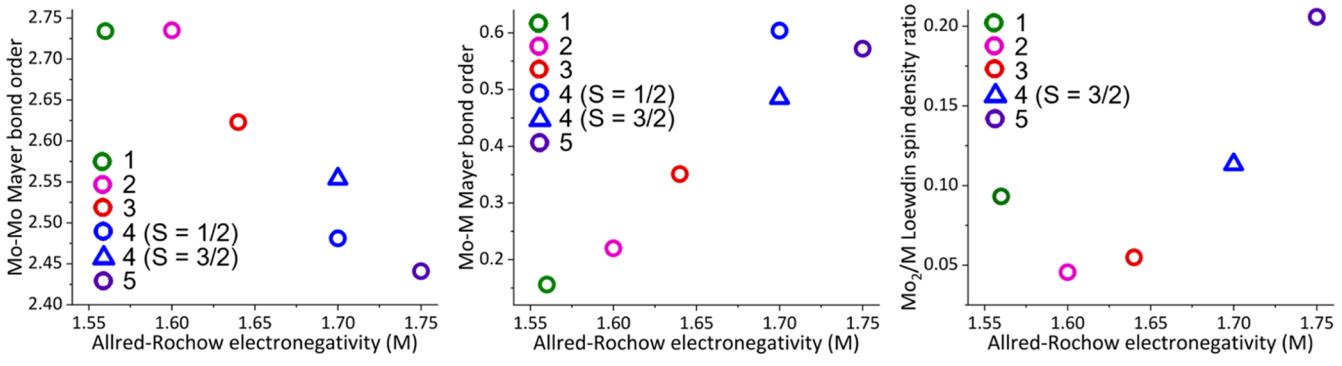

Figure 8. Plots of the Mo≣Mo (left) and Mo−M (center) MBO v. Allred−Rochow electronegativity of the heterometal ion (M). Right: Ratio of the outer Mo atom and heterometal ion Löwdin spin densities.

influence of the identity of the heterometal ion on the 3c/3e$^-$ metal−metal bond covalency. The leftmost and center plots in Figure 8 show the calculated Mo≣Mo and Mo−M MBOs, respectively, plotted versus the heterometal electronegativity χ, which is directly proportional to Z_{eff}.[46,107] The calculated Mo−Mo MBO values between 2 and 3 indicate a significant weakening from a true Mo≣Mo quadruple bond,[108] and Mo−M MBO values < 1 but non-zero indicate partial σ bonding. Most importantly, we observe a concomitant decrease in the Mo≣Mo MBO and increase in the Mo_2−M MBO with

https://doi.org/10.1021/acs.inorgchem.2c02118
Inorg. Chem. 2022, 61, 15058−15069

increasing χ of the heterometal ion. These trends demonstrate a shift of the electron density associated with the 3c/3e$^-$ σ bond toward the heterometal ion and therefore an increase in heterometallic metal−metal bond covalency. As outlined in the Introduction, this trend in heterometallic bonding is opposite of that based purely on polarity expectations—for Mo−Cr, having a smaller $\Delta\chi_{Mo-Cr} = 0.26$, the bonding interaction is the weakest, while the Mo−Ni interaction is strongest despite the larger $\Delta\chi_{Mo-Ni} = 0.45$. This *umpolung* of the heterometallic bond from initial expectation is due to the fact that the strong Mo≡Mo bond yields a low-energy, σ-symmetry electron pair that acts as a ligand to the third metal. Rather than behaving as a typical early, electropositive transition metal, the Mo_2 unit has bond polarity characteristics that are more like those of late, relatively electronegative transition metals like Pt.

Just as the vinoxy radical is described by limiting resonance structures **I** and **II**, we can propose resonance forms **III** and **IV** for Mo_2−M HEMACs, where the σ bonding can be localized to either the Mo−M(**III**) or the Mo−Mo(**IV**) interaction (Scheme 3). The π and δ bonds remain localized to the Mo_2 unit, and only the d_{z^2} spin of M is indicated. We anticipate that both resonance forms **III** and **IV** contribute to the Mo_2−M HEMAC series, with greater contribution from form **III** as M is changed from Cr to Mn to Fe to Co to Ni.

Scheme 3. Resonance Forms of the Vinoxy vs the Mo_2−M 3c/3e$^-$ Bonding System

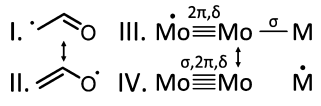

As highlighted in Scheme 3, the distribution of σ-symmetry spin is expected to change with the metal atom identity as well. Like the π non-bonding orbital of the vinoxy radical, we predicted that the σ_{nb} orbital of HEMAC complexes would show an increase in the spin density localized to the terminal Mo atom with an increase in the Z_{eff} of the heterometal ion. The rightmost plot in Figure 8 shows the ratio of the calculated Löwdin spin densities of the terminal Mo atom and the heterometal ion in **1**−**3**, **4** ($S = 3/2$), and **5** versus the heterometal χ (Table S5). The calculated spin density ratios show a consistent increase from M′ = Mn to Ni, indicating an increase in the localization of paramagnetic character on the terminal Mo atom with an increase of heterometal χ. The relatively large Mo/M′ spin density ratio for **1** can be rationalized in light of the fact that both the crystallographic and calculated structures of **1** have exceptionally short Mo−Cr distances, resulting in a greater degree of bond covalency that what would be independently predicted from the M′ identity alone. The increase in spin density with increasing M′ χ also suggests that the outer Mo atom in HEMACs with relatively covalent Mo−M′ bonds (i.e., **4** and **5**) could engage in radical-like chemical reactivity, a possibility we intend to explore in future work.

CONCLUSIONS

This work aimed to answer two questions that have underpinned previous studies of HEMAC systems: can a metal−metal quadruple bond serve as a dative ligand to a transition metal ion and result in an *umpolung* of the heterometallic interaction, and can we use the characteristics of that transition metal ion to modulate the covalency of the heterometallic interactions? This work now serves as a verification of those hypotheses via a systematic preparation and characterization of a series of $Mo_2M(dpa)_4(OTf)_2$ (M = Cr, Mn, Fe, Co, Ni) HEMACs. The synthetic route that previously afforded **5** was used to prepare **1**, **3**, and **4**, and we also report an improved synthetic route to the anhydrous $M(OTf)_2$ salts of Cr - Ni. Crystallographic and physical measurements of **1**, **2**, **3**, and **4** allow assignment of the heterometal ions as high spin species with the exception of **4**, which displays incomplete spin-crossover behavior. The negative measured and calculated values of D for **1** and **3** are attributed to the large easy-axis magnetic anisotropy that the Mo≡Mo quadruple bond enforces on the heterometal ion. Electronic structure calculations of the $Mo_2M(dpa)_4(OTf)_2$ HEMACs support the presence of a σ symmetry 3c/3e$^-$ bond that is delocalized across the entire metal-atom chain. The extent of this delocalization increases with increasing Z_{eff} of the heterometal ion (Cr < Mn < Fe < Co < Ni), as systematized in a linear trend in heterometallic bond order against Allred−Rochow electronegativity, χ. This trend is opposite to the expectation for bonding of these metals to a typical early transition metal ion, indicating that the strong Mo≡Mo quadruple bond causes an *umpolung* of the heterometallic 3c/3e$^-$ bond and is analogous to the π bonding in the vinoxy radical. Such effects can be used in future design of HEMAC compounds to tune the heterometallic covalency and stability and guide future synthetic efforts at accessing novel trimetallic chains. Ultimately, these findings provide new tools to understand the electronic structure of multimetallic systems. These tools can also be applied to fields of mixed-metal heterogenous (ad-atom or single-atom) catalysis[109,110] and biology in the realm of metalloenzymes. For example, it is notable that the Mo−Fe distances in **3** and **8** are similar to the Mo−Fe distance in the FeMo cofactor of nitrogenase, which contains several iron atoms and a Mo site.[80,111−113] We also anticipate the results reported here to be explored within the context of base metal catalysis, as we demonstrate earth-abundant base metals to be ennobled by the presence of a neighboring metal−metal bond.

ASSOCIATED CONTENT

Supporting Information

The Supporting Information is available free of charge at https://pubs.acs.org/doi/10.1021/acs.inorgchem.2c02118.

Cartesian coordinates (ZIP)

Experimental details, additional characterization data, and computational methods (PDF)

Accession Codes

CCDC 2159725−2159728 contain the supplementary crystallographic data for this paper. These data can be obtained free of charge via www.ccdc.cam.ac.uk/data_request/cif, or by emailing data_request@ccdc.cam.ac.uk, or by contacting The Cambridge Crystallographic Data Centre, 12 Union Road, Cambridge CB2 1EZ, UK; fax: +44 1223 336033.

AUTHOR INFORMATION

Corresponding Author

John. F. Berry − *Department of Chemistry, University of Wisconsin−Madison, Madison, Wisconsin 53706, United States;* orcid.org/0000-0002-6805-0640; Email: berry@chem.wisc.edu

Authors

Amelia M. Wheaton − *Department of Chemistry, University of Wisconsin−Madison, Madison, Wisconsin 53706, United States;* orcid.org/0000-0002-7743-9922

Jill A. Chipman − *Department of Chemistry, University of Wisconsin−Madison, Madison, Wisconsin 53706, United States;* orcid.org/0000-0002-3243-8766

Michael D. Roy − *Department of Chemistry, University of Wisconsin−Madison, Madison, Wisconsin 53706, United States*

Complete contact information is available at: https://pubs.acs.org/10.1021/acs.inorgchem.2c02118

Notes

The authors declare no competing financial interest.

■ ACKNOWLEDGMENTS

We thank the US National Science Foundation for supporting this work via CHE-1953924. The Bruker ImpactTM II MALDI mass spectrometer and the Bruker Quazar APEXII diffractometer were supported by a generous gift from Paul J. and Margaret M. Bender. The Bruker EleXsys E500 EPR spectrometer was supported by NSF CHE-0741901. The SeeCo Mössbauer spectrometer with a Janis SHI-850 4K cryostat and the Quantum Design MPMS3 SQUID magnetometer with an EverCool System were additionally supported by the UW-Madison Department of Chemistry. MO graphics were generated with UCSF Chimera, developed by the Resource for Biocomputing, Visualization, and Informatics at the University of California, San Francisco, with support from NIH grant P41-GM103311.

■ DEDICATION

We dedicate this work in memory of Prof. Carlos A. Murillo, who was an exceptional synthetic chemist, friend, and mentor.

■ REFERENCES

(1) Jencks, W. P. General acid-base catalysis of complex reactions in water. *Chem. Rev.* **1972**, *72*, 705−718.

(2) Staib, A.; Borgis, D.; Hynes, J. T. Proton transfer in hydrogen-bonded acid-base complexes in polar solvents. *J. Chem. Phys.* **1995**, *102*, 2487−2505.

(3) Pearson, R. G. Hard and soft acids and bases, HSAB, part 1: Fundamental principles. *J. Chem. Educ.* **1968**, *45*, 581.

(4) Pearson, R. G. Hard and soft acids and bases, HSAB, part II: Underlying theories. *J. Chem. Educ.* **1968**, *45*, 643.

(5) Mullins, J. J. Six pillars of organic chemistry. *J. Chem. Educ.* **2008**, *85*, 83.

(6) Holland, M. C.; Gilmour, R. Deconstructing covalent organocatalysis. *Angew. Chem., Int. Ed.* **2015**, *54*, 3862−3871.

(7) Greeley, J.; Mavrikakis, M. Alloy catalysts designed from first principles. *Nat. Mater.* **2004**, *3*, 810−815.

(8) Marvel, M. R.; Lesage, J.; Baek, J.; Halasyamani, P. S.; Stern, C. L.; Poeppelmeier, K. R. Cation−Anion Interactions and Polar Structures in the Solid State. *J. Am. Chem. Soc.* **2007**, *129*, 13963−13969.

(9) Woomer, A. H.; Druffel, D. L.; Sundberg, J. D.; Pawlik, J. T.; Warren, S. C. Bonding in 2D Donor-Acceptor Heterostructures. *J. Am. Chem. Soc.* **2019**, *141*, 10300−10308.

(10) Karas, L. J.; Wu, C. H.; Das, R.; Wu, J. I. Hydrogen bond design principles. *Wiley Interdiscip. Rev.: Comput. Mol. Sci.* **2020**, *10*, No. e1477.

(11) Schäfer, H. On the Problem of Polar Intermetallic Compounds: The Stimulation of E. Zintl's Work for the Modern Chemistry of Intermetallics. *Annu. Rev. Mater. Sci.* **1985**, *15*, 1−42.

(12) Oelkers, B.; Butovskii, M. V.; Kempe, R. f-Element-Metal Bonding and the Use of the Bond Polarity To Build Molecular Intermetalloids. *Chemistry* **2012**, *18*, 13566−13579.

(13) Belkova, N. V.; Epstein, L. M.; Filippov, O. A.; Shubina, E. S. Hydrogen and Dihydrogen Bonds in the Reactions of Metal Hydrides. *Chem. Rev.* **2016**, *116*, 8545−8587.

(14) Luca, O. R.; Crabtree, R. H. Redox-active ligands in catalysis. *Chem. Soc. Rev.* **2013**, *42*, 1440−1459.

(15) Singh, S. K.; Eng, J.; Atanasov, M.; Neese, F. Covalency and chemical bonding in transition metal complexes: An ab initio based ligand field perspective. *Coord. Chem. Rev.* **2017**, *344*, 2−25.

(16) Elsby, M. R.; Baker, R. T. Strategies and mechanisms of metal-ligand cooperativity in first-row transition metal complex catalysts. *Chem. Soc. Rev.* **2020**, *49*, 8933−8987.

(17) Norman, N. C.; Pringle, P. G. In defence of oxidation states. *Dalton Trans.* **2021**, *51*, 400−410.

(18) Nandi, A.; Kozuch, S. History and Future of Dative Bonds. *Chemistry* **2020**, *26*, 759−772.

(19) Green, M. L. H.; Parkin, G. Application of the Covalent Bond Classification Method for the Teaching of Inorganic Chemistry. *J. Chem. Educ.* **2014**, *91*, 807−816.

(20) Corey, E. J.; Seebach, D. Synthesis of 1,n-Dicarbonyl Derivates Using Carbanions from 1,3-Dithianes. *Angew. Chem., Int. Ed.* **1965**, *4*, 1077−1078.

(21) Gröbel, B.-T.; Seebach, D. Umpolung of the reactivity of carbonyl compounds through sulfur-containing reagents. *Synthesis* **1977**, *1977*, 357−402.

(22) Seebach, D. Methods of reactivity umpolung. *Angew. Chem., Int. Ed.* **1979**, *18*, 239−258.

(23) Eymur, S. Umpolung strategy: Advances in catalytic C-C bond formations. *Turk. J. Chem.* **2013**, *37*, 586.

(24) Tapia-Pineda, A.; Perez-Arrieta, C.; Silva-Cuevas, C.; Paleo, E.; Lujan-Montelongo, J. A. The Two Faces of Sulfinates: Illustrating Umpolung Reactivity. *J. Chem. Educ.* **2016**, *93*, 1470−1474.

(25) Hari, D. P.; Caramenti, P.; Waser, J. Cyclic Hypervalent Iodine Reagents: Enabling Tools for Bond Disconnection via Reactivity Umpolung. *Acc. Chem. Res.* **2018**, *51*, 3212−3225.

(26) Dai, X. J.; Li, C. C.; Li, C. J. Carbonyl umpolung as an organometallic reagent surrogate. *Chem. Soc. Rev.* **2021**, *50*, 10733−10742.

(27) Kan, J.; Chen, Z.; Qiu, Z.; Lv, L.; Li, C.; Li, C.-J. Umpolung carbonyls enable direct allylation and olefination of carbohydrates. *Sci. Adv.* **2022**, *8*, No. eabm6840.

(28) Flanigan, D. M.; Romanov-Michailidis, F.; White, N. A.; Rovis, T. Organocatalytic Reactions Enabled by N-Heterocyclic Carbenes. *Chem. Rev.* **2015**, *115*, 9307−9387.

(29) Vogel, P.; Lam, Y.-h.; Simon, A.; Houk, K. Organocatalysis Fundamentals and Comparisons to Metal and Enzyme Catalysis. *Catalysts* **2016**, *6*, 128.

(30) Wang, M. H.; Scheidt, K. A. Cooperative Catalysis and Activation with N-Heterocyclic Carbenes. *Angew. Chem., Int. Ed.* **2016**, *55*, 14912−14922.

(31) Wang, S.; König, B. Catalytic Generation of Carbanions through Carbonyl Umpolung. *Angew. Chem., Int. Ed.* **2021**, *60*, 21624−21634.

(32) Bugaut, X.; Glorius, F. Organocatalytic umpolung: N-heterocyclic carbenes and beyond. *Chem. Soc. Rev.* **2012**, *41*, 3511−3522.

(33) Warren, T. H.; Erker, G. Radical frustrated Lewis pairs. *Frustrated Lewis Pairs II*; Springer, 2013; pp 219−238.

(34) Stephan, D. W. A Tale of Two Elements: The Lewis Acidity/Basicity Umpolung of Boron and Phosphorus. *Angew. Chem., Int. Ed.* **2017**, *56*, 5984−5992.

(35) Jones, J. S.; Gabbaï, F. P. Coordination- and Redox-Noninnocent Behavior of Ambiphilic Ligands Containing Antimony. *Acc. Chem. Res.* **2016**, *49*, 857−867.

(36) Budy, H.; Gilmer, J.; Trageser, T.; Wagner, M. Anionic Organoboranes: Delicate Flowers Worth Caring for. *Eur. J. Inorg. Chem.* **2020**, *2020*, 4148−4162.

(37) Coste, S. C.; Pearson, T. J.; Altman, A. B.; Klein, R. A.; Finney, B. A.; Hu, M. Y.; Alp, E. E.; Vlaisavljevich, B.; Freedman, D. E. Orbital energy mismatch engenders high-spin ground states in heterobimetallic complexes. *Chem. Sci.* **2020**, *11*, 9971−9977.
(38) Krogman, J. P.; Thomas, C. M. Metal-metal multiple bonding in C_3-symmetric bimetallic complexes of the first row transition metals. *Chem. Commun.* **2014**, *50*, 5115−5127.
(39) Campos, J. Bimetallic cooperation across the periodic table. *Nat. Rev. Chem.* **2020**, *4*, 696−702.
(40) Chipman, J. A.; Berry, J. F. Paramagnetic Metal-Metal Bonded Heterometallic Complexes. *Chem. Rev.* **2020**, *120*, 2409−2447.
(41) Hua, S.-A.; Cheng, M.-C.; Chen, C.-h.; Peng, S.-M. From Homonuclear Metal String Complexes to Heteronuclear Metal String Complexes. *Eur. J. Inorg. Chem.* **2015**, *2015*, 2510−2523.
(42) Gade, L. H. Highly Polar Metal-Metal Bonds in "Early-Late" Heterodimetallic Complexes. *Angew. Chem., Int. Ed.* **2000**, *39*, 2658−2678.
(43) Buchwalter, P.; Rosé, J.; Braunstein, P. Multimetallic catalysis based on heterometallic complexes and clusters. *Chem. Rev.* **2015**, *115*, 28−126.
(44) Takamori, A.; Uemura, K. Dimerization of Paramagnetic Trinuclear Complexes by Coordination Geometry Changes Showing Mixed Valency and Significant Antiferromagnetic Coupling through −Pt···Pt− Bonds. *Inorg. Chem.* **2022**, *61*, 5762−5778.
(45) Eisenhart, R. J.; Clouston, L. J.; Lu, C. C. Configuring bonds between first-row transition metals. *Acc. Chem. Res.* **2015**, *48*, 2885−2894.
(46) Allred, A.; Rochow, E. G. A scale of electronegativity based on electrostatic force. *J. Inorg. Nucl. Chem.* **1958**, *5*, 264−268.
(47) Greenwood, B. P.; Rowe, G. T.; Chen, C.-H.; Foxman, B. M.; Thomas, C. M. Metal−Metal Multiple Bonds in Early/Late Heterobimetallics Support Unusual Trigonal Monopyramidal Geometries at both Zr and Co. *J. Am. Chem. Soc.* **2010**, *132*, 44−45.
(48) Zhou, W.; Saper, N. I.; Krogman, J. P.; Foxman, B. M.; Thomas, C. M. Effect of ligand modification on the reactivity of phosphinoamide-bridged heterobimetallic Zr/Co complexes. *Dalton Trans.* **2014**, *43*, 1984−1989.
(49) Gramigna, K. M.; Dickie, D. A.; Foxman, B. M.; Thomas, C. M. Cooperative H_2 Activation across a Metal−Metal Multiple Bond and Hydrogenation Reactions Catalyzed by a Zr/Co Heterobimetallic Complex. *ACS Catal.* **2019**, *9*, 3153−3164.
(50) Eisenhart, R. J.; Rudd, P. A.; Planas, N.; Boyce, D. W.; Carlson, R. K.; Tolman, W. B.; Bill, E.; Gagliardi, L.; Lu, C. C. Pushing the Limits of Delta Bonding in Metal-Chromium Complexes with Redox Changes and Metal Swapping. *Inorg. Chem.* **2015**, *54*, 7579−7592.
(51) Clouston, L. J.; Bernales, V.; Cammarota, R. C.; Carlson, R. K.; Bill, E.; Gagliardi, L.; Lu, C. C. Heterobimetallic Complexes That Bond Vanadium to Iron, Cobalt, and Nickel. *Inorg. Chem.* **2015**, *54*, 11669−11679.
(52) Tereniak, S. J.; Carlson, R. K.; Clouston, L. J.; Young, V. G., Jr.; Bill, E.; Maurice, R.; Chen, Y. S.; Kim, H. J.; Gagliardi, L.; Lu, C. C. Role of the metal in the bonding and properties of bimetallic complexes involving manganese, iron, and cobalt. *J. Am. Chem. Soc.* **2014**, *136*, 1842−1855.
(53) Rudd, P. A.; Liu, S.; Planas, N.; Bill, E.; Gagliardi, L.; Lu, C. C. Multiple metal-metal bonds in iron-chromium complexes. *Angew. Chem., Int. Ed.* **2013**, *52*, 4449−4452.
(54) Clouston, L. J.; Siedschlag, R. B.; Rudd, P. A.; Planas, N.; Hu, S.; Miller, A. D.; Gagliardi, L.; Lu, C. C. Systematic variation of metal-metal bond order in metal-chromium complexes. *J. Am. Chem. Soc.* **2013**, *135*, 13142−13148.
(55) Wu, B.; Wilding, M. J.; Kuppuswamy, S.; Bezpalko, M. W.; Foxman, B. M.; Thomas, C. M. Exploring Trends in Metal-Metal Bonding, Spectroscopic Properties, and Conformational Flexibility in a Series of Heterobimetallic Ti/M and V/M Complexes (M = Fe, Co, Ni, and Cu). *Inorg. Chem.* **2016**, *55*, 12137−12148.
(56) Wu, B.; Gramigna, K. M.; Bezpalko, M. W.; Foxman, B. M.; Thomas, C. M. Heterobimetallic Ti/Co Complexes That Promote Catalytic N-N Bond Cleavage. *Inorg. Chem.* **2015**, *54*, 10909−10917.
(57) Barden, B. A.; Culcu, G.; Krogman, J. P.; Bezpalko, M. W.; Hatzis, G. P.; Dickie, D. A.; Foxman, B. M.; Thomas, C. M. Assessing the Metal-Metal Interactions in a Series of Heterobimetallic Nb/M Complexes (M = Fe, Co, Ni, Cu) and Their Effect on Multielectron Redox Properties. *Inorg. Chem.* **2019**, *58*, 821−833.
(58) Beach, S. A.; Zuckerman, L. A.; Portillo, R. I.; Shores, M. P.; Rheingold, A. L.; Doerrer, L. H. Heterobimetallic {PtMn} and {PtFe} lantern complexes with exceptionally long metallophilic contacts. *Inorg. Chim. Acta* **2019**, *493*, 81−90.
(59) Baddour, F. G.; Fiedler, S. R.; Shores, M. P.; Bacon, J. W.; Golen, J. A.; Rheingold, A. L.; Doerrer, L. H. Pt···Pt vs Pt···S Contacts Between Pt-Containing Heterobimetallic Lantern Complexes. *Inorg. Chem.* **2013**, *52*, 13562−13575.
(60) Rohmer, M.-M.; Strich, A.; Bénard, M.; Malrieu, J.-P. Metal−Metal Bond Length Variability in Co_3(dipyridylamide)$_4Cl_2$: Bond-Stretch Isomerism, Crystal Field Effects, or Spin Transition Process? A DFT Study. *J. Am. Chem. Soc.* **2001**, *123*, 9126−9134.
(61) Sun, G.; Zheng, X.; Xu, K.; Song, Y.; Zhang, J. Photodissociation Dynamics of Vinoxy Radical via the B(2)A″ State: The H + CH_2CO Product Channel. *J. Phys. Chem. A* **2021**, *125*, 8882−8890.
(62) Nippe, M.; Berry, J. F. Introducing a Metal−Metal Multiply Bonded Group as an "Axial Ligand" to Iron: Synthetic Design of a Linear Cr−Cr···Fe Framework. *J. Am. Chem. Soc.* **2007**, *129*, 12684−12685.
(63) Brogden, D. W.; Christian, J. H.; Dalal, N. S.; Berry, J. F. Completing the series of Group VI heterotrimetallic $M_2Cr(dpa)_4Cl_2$ (M_2 = Cr_2, Mo_2, MoW and W_2) compounds and investigating their metal−metal interactions using density functional theory. *Inorg. Chim. Acta* **2015**, *424*, 241−247.
(64) Brogden, D. W.; Berry, J. F. Heterometallic Multiple Bonding: Delocalized Three-Center σ and π Bonding in Chains of 4d and 5d Transition Metals. *Inorg. Chem.* **2014**, *53*, 11354−11356.
(65) Nippe, M.; Turov, Y.; Berry, J. F. Remote effects of axial ligand substitution in heterometallic Cr identical with Cr···M chains. *Inorg. Chem.* **2011**, *50*, 10592−10599.
(66) Nippe, M.; Bill, E.; Berry, J. F. Group 6 complexes with iron and zinc heterometals: understanding the structural, spectroscopic, and electrochemical properties of a complete series of M≡M···M' compounds. *Inorg. Chem.* **2011**, *50*, 7650−7661.
(67) Nippe, M.; Victor, E.; Berry, J. F. Do Metal-Metal Multiply-Bonded "Ligands" Have a trans Influence? Structural and Magnetic Comparisons of Heterometallic Cr≡Cr···Co and Mo≡Mo···Co Interactions. *Eur. J. Inorg. Chem.* **2008**, *2008*, 5569−5572.
(68) Arcisauskaite, V.; Spivak, M.; McGrady, J. E. Structure and bonding in trimetallic arrays containing a Cr-Cr quadruple bond: A challenge to density functional theory. *Inorg. Chim. Acta* **2015**, *424*, 293−299.
(69) Spivak, M.; López, X.; de Graaf, C. Trends in the Bond Multiplicity of Cr_2, Cr_3, and Cr_2M (M = Zn, Ni, Fe, Mn) Complexes Extracted from Multiconfigurational Wave Functions. *J. Phys. Chem. A* **2019**, *123*, 1538−1547.
(70) Chipman, J. A.; Berry, J. F. Facile Axial Ligand Substitution in Linear Mo≡Mo-Ni Complexes. *Inorg. Chem.* **2018**, *57*, 9354−9363.
(71) Guan, E.; Ciston, J.; Bare, S. R.; Runnebaum, R. C.; Katz, A.; Kulkarni, A.; Kronawitter, C. X.; Gates, B. C. Supported Metal Pair-Site Catalysts. *ACS Catal.* **2020**, *10*, 9065−9085.
(72) Ro, I.; Resasco, J.; Christopher, P. Approaches for Understanding and Controlling Interfacial Effects in Oxide-Supported Metal Catalysts. *ACS Catal.* **2018**, *8*, 7368−7387.
(73) Blair, D. F.; Bocian, D. F.; Babcock, G. T.; Chan, S. I. Evidence for modulation of the heme absorptions of cytochrome c oxidase by metal-metal interactions. *Biochemistry* **1982**, *21*, 6928−6935.
(74) Blackburn, N. J.; Barr, M. E.; Woodruff, W. H.; van der Ooost, J.; de Vries, S. Metal-Metal Bonding in Biology: EXAFS Evidence for a 2.5 .ANG. Copper-Copper Bond in the CuA Center of Cytochrome Oxidase. *Biochemistry* **1994**, *33*, 10401−10407.
(75) Holm, R. H.; Kennepohl, P.; Solomon, E. I. Structural and functional aspects of metal sites in biology. *Chem. Rev.* **1996**, *96*, 2239−2314.

https://doi.org/10.1021/acs.inorgchem.2c02118
Inorg. Chem. 2022, 61, 15058−15069

(76) Ogata, H.; Kellers, P.; Lubitz, W. The crystal structure of the [NiFe] hydrogenase from the photosynthetic bacterium Allochromatium vinosum: characterization of the oxidized enzyme (Ni-A state). *J. Mol. Biol.* **2010**, *402*, 428−444.
(77) Amara, P.; Mouesca, J. M.; Volbeda, A.; Fontecilla-Camps, J. C. Carbon Monoxide Dehydrogenase Reaction Mechanism: A Likely Case of Abnormal CO_2 Insertion to a Ni−H− Bond. *Inorg. Chem.* **2011**, *50*, 1868−1878.
(78) Lindahl, P. A. Metal-metal bonds in biology. *J. Inorg. Biochem.* **2012**, *106*, 172−178.
(79) Spatzal, T.; Perez, K. A.; Einsle, O.; Howard, J. B.; Rees, D. C. Ligand binding to the FeMo-cofactor: structures of CO-bound and reactivated nitrogenase. *Science* **2014**, *345*, 1620−1623.
(80) Bjornsson, R.; Neese, F.; DeBeer, S. Revisiting the Mössbauer Isomer Shifts of the FeMoco Cluster of Nitrogenase and the Cofactor Charge. *Inorg. Chem.* **2017**, *56*, 1470−1477.
(81) Blomberg, M. R. A. The structure of the oxidized state of cytochrome c oxidase - experiments and theory compared. *J. Inorg. Biochem.* **2020**, *206*, 111020.
(82) Bozic-Weber, B.; Constable, E. C.; Housecroft, C. E. Light harvesting with Earth abundant d-block metals: Development of sensitizers in dye-sensitized solar cells (DSCs). *Coord. Chem. Rev.* **2013**, *257*, 3089−3106.
(83) Fukuzumi, S.; Lee, Y.-M.; Nam, W. Thermal and photocatalytic production of hydrogen with earth-abundant metal complexes. *Coord. Chem. Rev.* **2018**, *355*, 54−73.
(84) Larsen, C. B.; Wenger, O. S. Photoredox Catalysis with Metal Complexes Made from Earth-Abundant Elements. *Chemistry* **2018**, *24*, 2039−2058.
(85) Wenger, O. S. Photoactive Complexes with Earth-Abundant Metals. *J. Am. Chem. Soc.* **2018**, *140*, 13522−13533.
(86) Zhao, H.; Xu, J.; Yin, D.; Du, Y. Electrolytes for Batteries with Earth-Abundant Metal Anodes. *Chemistry* **2018**, *24*, 18220−18234.
(87) Förster, C.; Heinze, K. Photophysics and photochemistry with Earth-abundant metals - fundamentals and concepts. *Chem. Soc. Rev.* **2020**, *49*, 1057−1070.
(88) Kondo, M.; Tatewaki, H.; Masaoka, S. Design of molecular water oxidation catalysts with earth-abundant metal ions. *Chem. Soc. Rev.* **2021**, *50*, 6790−6831.
(89) Lawrance, G. A. Coordinated trifluoromethanesulfonate and fluorosulfate. *Chem. Rev.* **1986**, *86*, 17−33.
(90) Boumizane, K.; Herzog-Cance, M.; Jones, D.; Pascal, J.; Potier, J.; Roziere, J. Synthesis, vibrational spectroscopy and EXAFS analysis of some divalent and trivalent trifluoromethanesulphonato complexes. *Polyhedron* **1991**, *10*, 2757−2769.
(91) Dixon, N. E.; Lawrance, G. A.; Lay, P. A.; Sargeson, A. M.; Taube, H. Introduction to Trifluoromethanesulfonates and Trifluoromethanesulfonato-O Complexes. *Inorganic Syntheses*; Wiley, 1986; pp 243−250.
(92) Oldengott, J.; Richthofen, C.-G.; Walleck, S.; Stammler, A.; Bögge, H.; Glaser, T. Trinuclear Triplesalophen Building Blocks with Terminal Cyanides and Implications for the Spin-Polarization Mechanism for Low-Spin Fe^{III} and Cr^{III} Ions. *Eur. J. Inorg. Chem.* **2018**, *2018*, 4987−4996.
(93) Coucouvanis, D. Reagents, Useful and Ligands. *Inorganic Syntheses*; Wiley, 2002; pp 75−121.
(94) Haynes, J. S.; Sams, J. R.; Thompson, R. C. Synthesis and structural studies of iron(II) and iron(III) sulfonates. *Can. J. Chem.* **1981**, *59*, 669−678.
(95) Haynes, J. S.; Sams, J. R.; Thompson, R. C. Low temperature magnetic and Mössbauer studies on anhydrous iron(II) sulfonates. *Can. J. Chem.* **1986**, *64*, 744−750.
(96) Nippe, M.; Victor, E.; Berry, J. F. Oxidation chemistry of axially protected Mo_2 and W_2 quadruply bonded compounds. *Inorg. Chem.* **2009**, *48*, 11889−11895.
(97) Dai, W.; Kim, S. B.; Pike, R. D.; Cahill, C. L.; Sweigart, D. A. Electrochemical Study of Manganese and Rhenium Arene Complexes $(C_6R_6)M(CO)_3^+$ (R = Me, Et). *Organometallics* **2010**, *29*, 5173−5178.
(98) Reginato, N.; Harrington, L. E.; Ortin, Y.; McGlinchey, M. J. Unexpectedly different reactions of $[(arene)Mn(CO)_3]^+$ cations (arene = trindane, indane, tetralin, or dibenzosuberane) with potassium t-butoxide — C−H insertions, haptotropic shifts, dimerization, or elimination. *Can. J. Chem.* **2009**, *87*, 232−246.
(99) Oh, M.; Reingold, J. A.; Carpenter, G. B.; Sweigart, D. A. Manganese tricarbonyl transfer (MTT) reagents in the construction of novel organometallic systems. *Coord. Chem. Rev.* **2004**, *248*, 561−569.
(100) Nippe, M.; Wang, J.; Bill, E.; Hope, H.; Dalal, N. S.; Berry, J. F. Crystals in which some metal atoms are more equal than others: inequalities from crystal packing and their spectroscopic/magnetic consequences. *J. Am. Chem. Soc.* **2010**, *132*, 14261−14272.
(101) Chipman, J. A.; Berry, J. F. Extraordinarily Large Ferromagnetic Coupling ($J \geq 150\ cm^{-1}$) by Electron Delocalization in a Heterometallic Mo≣Mo−Ni Chain Complex. *Chem.—Eur. J.* **2018**, *24*, 1494−1499.
(102) Solomon, E. I.; Brunold, T. C.; Davis, M. I.; Kemsley, J. N.; Lee, S.-K.; Lehnert, N.; Neese, F.; Skulan, A. J.; Yang, Y.-S.; Zhou, J. Geometric and electronic structure/function correlations in non-heme iron enzymes. *Chem. Rev.* **2000**, *100*, 235−350.
(103) Solomon, E. I.; Pavel, E. G.; Loeb, K. E.; Campochiaro, C. Magnetic circular dichroism spectroscopy as a probe of the geometric and electronic structure of non-heme ferrous enzymes. *Coord. Chem. Rev.* **1995**, *144*, 369−460.
(104) Trautwein, A. X.; Bill, E.; Bominaar, E. L.; Winkler, H. Iron-containing proteins and related analogs - complementary Mössbauer, EPR and magnetic susceptibility studies. *Bioinorganic Chemistry*; Springer, 1991; pp 1−95.
(105) Christian, J. H.; Brogden, D. W.; Bindra, J. K.; Kinyon, J. S.; van Tol, J.; Wang, J.; Berry, J. F.; Dalal, N. S. Enhancing the Magnetic Anisotropy of Linear Cr(II) Chain Compounds Using Heavy Metal Substitutions. *Inorg. Chem.* **2016**, *55*, 6376−6383.
(106) Chipman, J. A. Modifications to M_2M' Heterometallic Chain Compounds and their Spectroscopic, Magnetic, and Electronic Consequences. Ph.D. Thesis, The University of Wisconsin−Madison, Ann Arbor, 2019.
(107) Accorinti, H.; Labarca, M. Commentary on the Models of Electronegativity. *J. Chem. Educ.* **2020**, *97*, 3474−3477.
(108) Li Manni, G.; Dzubak, A. L.; Mulla, A.; Brogden, D. W.; Berry, J. F.; Gagliardi, L. Assessing metal-metal multiple bonds in Cr-Cr, Mo-Mo, and W-W compounds and a hypothetical U-U compound: a quantum chemical study comparing DFT and multireference methods. *Chemistry* **2012**, *18*, 1737−1749.
(109) Hannagan, R. T.; Giannakakis, G.; Flytzani-Stephanopoulos, M.; Sykes, E. C. H. Single-Atom Alloy Catalysis. *Chem. Rev.* **2020**, *120*, 12044−12088.
(110) Kaiser, S. K.; Chen, Z.; Faust Akl, D.; Mitchell, S.; Pérez-Ramírez, J. Single-Atom Catalysts across the Periodic Table. *Chem. Rev.* **2020**, *120*, 11703−11809.
(111) Buscagan, T. M.; Rees, D. C. Rethinking the Nitrogenase Mechanism: Activating the Active Site. *Joule* **2019**, *3*, 2662−2678.
(112) Tanifuji, K.; Ohki, Y. Metal-Sulfur Compounds in N_2 Reduction and Nitrogenase-Related Chemistry. *Chem. Rev.* **2020**, *120*, 5194−5251.
(113) Van Stappen, C.; Decamps, L.; Cutsail, G. E., 3rd; Bjornsson, R.; Henthorn, J. T.; Birrell, J. A.; DeBeer, S. The Spectroscopy of Nitrogenases. *Chem. Rev.* **2020**, *120*, 5005−5081.

https://doi.org/10.1021/acs.inorgchem.2c02118
Inorg. Chem. 2022, 61, 15058−15069